Received: 17 October 2023 | Revised: 15 April 2024 | Accepted: 17 May 2024

DOI: 10.1111/jmi.13334

Journal of Microscopy RMS

ORIGINAL ARTICLE

Smartphone-based optical sectioning (SOS) microscopy with a telecentric design for fluorescence imaging

Ziao Jiao[1,2] | Mingliang Pan[1] | Khadija Yousaf[3] | Daniel Doveiko[3] | Michelle Maclean[1,4] | David Griffin[1] | Yu Chen[3] | David Day Uei Li[1,2]

[1]Department of Biomedical Engineering, University of Strathclyde, Glasgow, Scotland, UK

[2]Strathclyde Institute of Pharmacy and Biomedical Sciences, University of Strathclyde, Glasgow, Scotland, UK

[3]Department of Physics, University of Strathclyde, Glasgow, Scotland, UK

[4]Department of Electronic & Electrical Engineering, The Robertson Trust Laboratory for Electronic Sterilisation Technologies (ROLEST), University of Strathclyde, Glasgow, UK

Correspondence
Ziao Jiao, Department of Biomedical Engineering, University of Strathclyde, Glasgow G1 1XQ, Scotland, UK.
Email: ziao.jiao@strath.ac.uk

Funding information
Engineering and Physical Sciences Research Council, Grant/Award Number: EP/L01596X/1; China Scholarship Council, Grant/Award Number: 202108060070

Abstract

We propose a smartphone-based optical sectioning (SOS) microscope based on the HiLo technique, with a single smartphone replacing a high-cost illumination source and a camera sensor. We built our SOS with off-the-shelf optical, mechanical cage systems with 3D-printed adapters to seamlessly integrate the smartphone with the SOS main body. The liquid light guide can be integrated with the adapter, guiding the smartphone's LED light to the digital mirror device (DMD) with neglectable loss. We used an electrically tuneable lens (ETL) instead of a mechanical translation stage to realise low-cost axial scanning. The ETL was conjugated to the objective lens's back pupil plane (BPP) to construct a telecentric design by a 4f configuration to maintain the lateral magnification for different axial positions. SOS has a 571.5 μm telecentric scanning range and an 11.7 μm axial resolution. The broadband smartphone LED torch can effectively excite fluorescent polystyrene (PS) beads. We successfully used SOS for high-contrast fluorescent PS beads imaging with different wavelengths and optical sectioning imaging of multilayer fluorescent PS beads. To our knowledge, the proposed SOS is the first smartphone-based HiLo optical sectioning microscopy (£1965), which can save around £7035 compared with a traditional HiLo system (£9000). It is a powerful tool for biomedical research in resource-limited areas.

KEYWORDS
HiLo microscopy, optical sectioning microscopy, smartphone microscopy

1 | INTRODUCTION

Widefield fluorescence microscopy (WFM) is commonly used to image biological samples due to its high cost-effectiveness, fast imaging speed, low photodamage and low photobleaching.[1–3] However, according to WFM's optical transfer function (OTF), the optical sectioning ability is poor, which means WFM images have low contrast due to out-of-focus signals.[4,5] Several methods have been proposed for obtaining high-contrast optical sectioning images. For instance, confocal laser scanning microscopy (CLSM) is realised by placing a spatial pinhole filter at the conjugated position of the illumination focus point to reject out-of-focus fluorescence, and the galvo mirror and the motorised stage are often used as a scanning mechanism for acquiring 3D images.[6–8] Line scanning confocal

microscopy (LSCM) is established based on a similar principle,[9,10] a slit replaces a spatial pinhole in CLSM, and samples are scanned in two directions instead of three to improve the scanning speed. Two-photon excitation microscopy is also an effective way to obtain high-contrast images. With near-infrared two-photon absorption, the scattering in tissues is minimised, and out-of-focus signals are strongly suppressed.[11–13] Light sheet microscopy (LSM) is a potent optical sectioning technique that employs orthogonal arrangements of the illumination and detection arms.[14–16] In LSM, the illumination arm and detection arm are separated orthogonally. This configuration enables the lens to primarily detect signals from the specifically illuminated plane, enhancing image clarity and reducing photobleaching and phototoxicity in the sample.[17–19]

Compared with the methods mentioned above, structured illumination microscopy (SIM) has a relatively simple configuration. This technique can provide modulated and in-focus images with high contrast and optical sectioning performances.[20] It can be realised by using a digital mirror device (DMD) or a spatial light modulator (SLM) to project periodic patterns on the sample plane.[21,22] To make the optical sectioning easily realised on WFM, Mertz's group developed HiLo microscopy.[23–25] Besides HiLo's simple configuration, only two images are required for HiLo instead of three for SIM.[24] Using the HiLo principle, we only need one uniform-illuminated image and one structured-illuminated image and use the image processing algorithms to obtain the optically sectioned image.[24] HiLo is cost-effective because it uses a coherent laser and a diffuser to create speckles on samples[23–25] or an incoherent light source and a DMD to project patterns on samples.[26,27] Lim et al.[25] have presented that HiLo's optical sectioning performance is comparable to CLSM.[24,25,28] It can be used in 3D image cytometers.[29] To observe neuron cell activities,[30,31] discover 3D cell mechanical properties,[32] and enhance retinal imaging quality.[33] HiLo can be applied to endoscopy[28,34] and optical scanning microscopy.[35,36] Although HiLo is relatively straightforward compared with other optical sectioning modalities, the cost of its light source, DMD or SLM, and advanced camera sensor is still significant.

Most smartphones have high-performance image sensors with camera lenses, and their costs are pretty low. Smartphone-based microscopy is, therefore, a powerful and low-cost option for bioimaging,[37–39] disease detection,[40,41] and point-of-care testing applications.[42] Furthermore, smartphones can be easily coupled with different imaging modalities, like bright-field microscopy,[43] fluorescence microscopy,[44,45] phase microscopy[46–49] and Fourier ptychographic microscopy.[50] However, most of these devices only utilise smartphones' camera lenses and imaging sensors; they still require additional LEDs as external illumination sources, not sufficiently liberating their powerful performances.[51–53] To further simplify smartphone-based microscopy, screen LCD and LED flashlights of smartphones have been used for illumination.[50,54]

Here, we propose smartphone-based optical sectioning (SOS) microscopy. To our knowledge, it is the first smartphone-based HiLo microscope that offers low-cost optically sectioned widefield imaging. The smartphone in our SOS microscope acts as a CMOS sensor to decrease the cost of traditional HiLo microscopes. High-resolution coloured images can be acquired without external colour filters because of the smartphone's Bayer filter and the small pixel size. We made adapters to integrate the smartphone into the main microscope body. We inserted a liquid light guide into the adapter to guide the smartphone's flashlight to the DMD. Meanwhile, a reverse smartphone lens was attached to the camera to conjugate the intermediate image plane into the smartphone's sensor with 1× magnification. The ETL was conjugated to the BPP of the objective lens to realise a telecentric axial scan and maintain constant lateral magnification at different depths. The smartphone's LED torch has a broadband spectrum, making it an effective excitation light source for imaging three different fluorescent polystyrene (PS) beads.

The SOS has a 571.5 μm telecentric scanning range and an 11.7 μm axial resolution. We used it to acquire high-contrast widefield fluorescent images of 10 μm PS beads with emission wavelengths 465, 515, and 605 nm. Optically sectioned images of multilayer PS beads were also obtained in a 25 μm axial range with a 5 μm step. The proposed system replaces a scientific camera, an illumination source, and a motorised stage (cost ~£9000) in the traditional HiLo microscope with a smartphone, a light guide, an electrically tuneable lens and several fixings for optical components (cost ~£1965+ several hundred pounds). This study demonstrates the potential of using a smartphone for optical sectioning microscopy. It paves the way for smaller, cheaper next-generation HiLo microscopy systems.

2 | MATERIALS AND METHODS

2.1 | Optical setup of the system

Figure 1A presents the SOS' optical configuration. A smartphone (iPhone 13Pro, Apple) provides illumination and detection for simplicity. For illumination, the LED light from the smartphone is first guided by a liquid light guide (3mm × 6', Edmund Optics), then filtered by the selected filter and collimated by the Köhler illumination setup (Section 2.3 for detail) before it illuminates the DMD (DLP LightCrafter 6500, Texas Instruments). The reflected light from the DMD then passes through the dichromatic mirror. The light emerging from the liquid waveguide is focused to a spot by the apochromatic

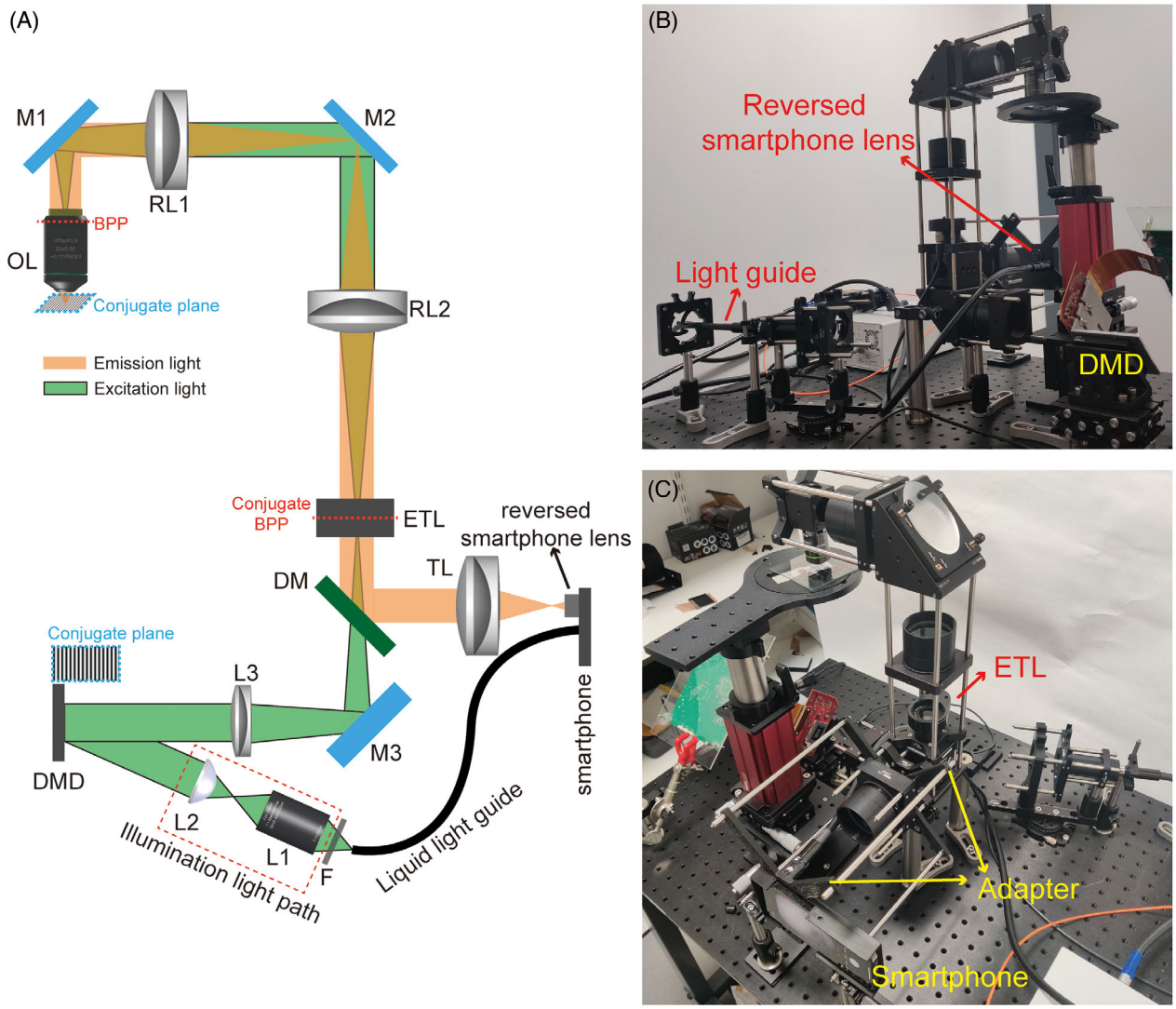

FIGURE 1 Optical setup of the proposed SOS microscope. (A) The diagram of the SOS microscope. The DMD plane, which is conjugated to the sample plane, is illuminated by the collimated light. L3, RL2 and RL1, OL consist of two 4f systems. The illumination is introduced at 24° to ensure the DMD can reflect the light at 0°. For telecentric design, the ETL is conjugated to the BPP. The image is recorded by a smartphone equipped with a reversed smartphone lens. (B), (C) The experiment setup. We designed adapters to integrate the smartphone with the SOS main body (Section 2.4 for detail). OL: objective lens; M1-M3: mirror; RL1-RL2, L1-L3: lens; F: filter; TL: tube lens; DM: dichromatic mirror; DMD: digital mirror device; ETL: electrical tuneable lens; BPP: back pupil plane.

collector lens L1 (MAP10303-A, Thorlabs) and collimated by L2 (ACL3026U-A, Thorlabs). Because each pixel on the DMD is activated along the diagonal line, the DMD is rotated at 45° to maintain the input and reflected light at the same plane (Figure 1B). Beyond that, the illumination light is introduced at 24° from the direction normal to the DMD to reflect the light in the programmed pixels at 0°. The DMD plane is conjugated to the sample plane by two 4f systems: L3-RL2 (L3: AC508-180A, RL2: AC508-100A, Thorlabs) and OL-RL1 (OL: UPLanSApo/20X/0.75, Olympus, RL1: AC508-100A, Thorlabs) for structured illumination. The ETL (EL-16-40-TC-VIS-5D-M27, Optotune), with a fast response, acts as a nonmechanical axial scanning device; it is conjugated to the back pupil plane (BPP) of the objective lens. This can guarantee the telecentric setup and maintain the constant lateral magnification during axial scanning (detailed in Section 2.2).

The objective lens collects the excited fluorescent signal, and the first image is located at the back focal plane of RL1. Then the image is again formed at the back focal plane of TL (AC508-180A, Thorlabs) through RL2-TL 4f system. The ETL is located at the confocal plane of RL2, TL and L3. To acquire the image using a smartphone, we put the same reversed smartphone lens (from eBay) in front of the camera to combine a 1:1 symmetric relay system. So, the image can finally be recorded by the smartphone sensor. The smartphone sensor is equipped with the Bayer filter to acquire coloured images directly. Furthermore, we design and fabricate adapters for integrating the smartphone and the liquid light guide to the cage system of the microscope's

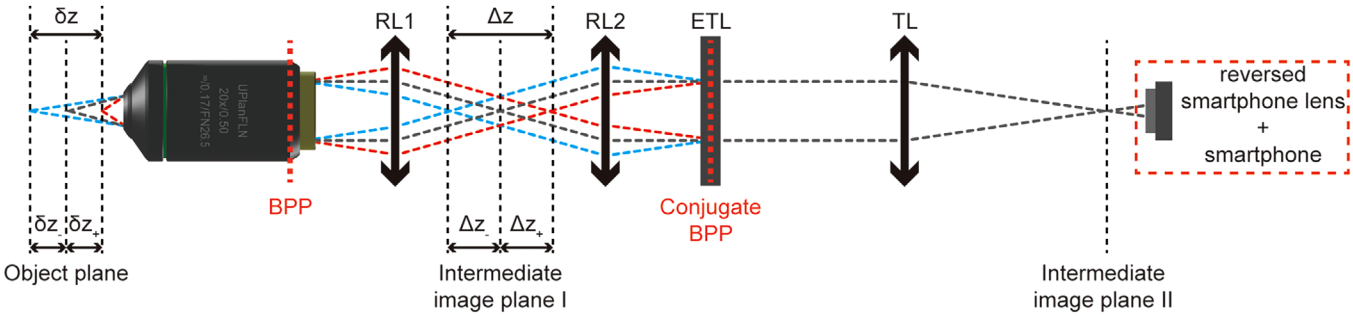

FIGURE 2 Telecentric imaging optical path. We configured RL1 and RL2 as a 4f system to relay the objective lens' back pupil plane to ETL. The red and blue lines depict the minimum and maximum axial scanning ranges.

main body. Therefore, the smartphone camera and lenses on the microscope's main body are concentric (Figure 1C; Section 2.4 for detail).

2.2 | Telecentric design and theoretical axial scanning range

The telecentric design can realise axial scanning with invariant lateral magnification. Here, we used an ETL for axial scanning by tuning the input current to change its surface shape. To maintain lateral magnification at different depths, the entrance and exit pupils should be located infinitely at object and image space, respectively. Therefore, the system setup should be strictly in the 4f configuration.

Figure 2 illustrates the telecentric design of the imaging path. ETL should be conjugated with the objective lens's back pupil plane (BPP) to obtain the telecentric design. It is hard to put ETL directly at BPP; therefore, we used the 4f configuration (RL1-RL2 lens pair) to relay BPP, at which ETL and BPP are conjugated. Meanwhile, ETL is also located at the front focal plane of the tube lens (TL) to guarantee that the image space is telecentric. We have to ensure that the conjugated BPP's aperture is smaller than the ETL's aperture. Here, the BPP diameter of the objective lens is 9 mm, and ETL's clear aperture size is 16 mm. We used RL1 and RL2 (both with 100 mm focal lengths) to combine a 1:1 4f configuration, and its confocal plane coincided with the intermediate image plane I.

The theoretical scanning range in the object space is determined by the relationship between the object plane's axial displacement δz_+ and the intermediate image plane Δz_+ as shown in Figure 2:

$$\delta z_+ = \frac{n_0}{n_i M_{OL-RL1}^2} \Delta z_+, \tag{1}$$

where M_{OL-RL1} is the lateral magnification of the objective lens and the first relay lens (RL1), n_0 and n_i are the refractive indices in the object and the image space, respectively. Here, for simplicity, both of them are unity. The actual scanning range is different depending on the sample's refractive index.

The intermediate image plane I can be tuned by ETL, and we can treat RL2 and ETL as a compound lens. According to Gullstrand's equation[55]:

$$f_{RL2-ETL} = \frac{f_{ETL} f_{RL2}}{f_{ETL} + f_{RL2} - d_{ETL-RL2}}, \tag{2}$$

where $f_{RL2-ETL}$ is the focal length of the RL2-ETL-compound lens, f_{ETL} and f_{RL2} are the focal lengths of ETL and RL, and $d_{ETL-RL2}$ is the distance between ETL and RL2. Since ETL is located at the back focal plane of RL2, Equation (2) can be rewritten as:

$$f_{RL2-ETL} = \frac{f_{ETL} f_{RL2}}{f_{ETL} + f_{RL2} - f_{RL2}} = f_{RL2}. \tag{3}$$

Therefore, tuning ETL's optical power changes the compound lens's front principal plane instead of changing its focal length. This is equivalent to the axial displacement of the intermediate image plane I. As shown in Figure 2, Δz_+ can be written as[55]:

$$\Delta z_+ = \frac{f_{RL2}^2}{f_{ETL}}, \tag{4}$$

Combining Equations (1) and (4) to obtain:

$$\delta z_+ = \frac{1}{M_{OL-RL1}^2} \times \frac{\phi_{ETL}}{\phi_{RL2}^2}, \tag{5}$$

where ϕ is the corresponding optical power.

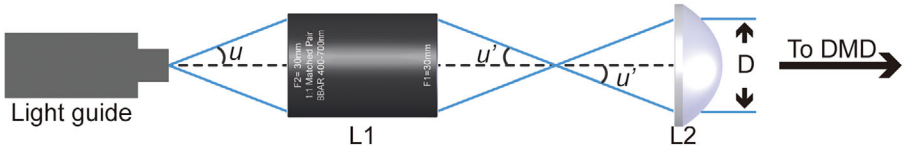

FIGURE 3 Collimated light path for illumination. L1 (MAP10303-A, Thorlabs), L2 (ACL3026U-A, Thorlabs). L1 has 1× magnification, and the NA of L2 is 0.55.

Therefore, the scanning range in the object space can be derived as:

$$\begin{aligned}\delta_z &= |\delta z_-| + |\delta z_+| \\ &= \frac{1}{M_{OL-RL1}^2}\left(\left|\frac{\phi_{ETL-\max}}{\phi_{RL2}^2}\right| + \left|\frac{\phi_{ETL-\min}}{\phi_{RL2}^2}\right|\right), \end{aligned} \quad (6)$$

where $\phi_{ETL-\min}$ and $\phi_{ETL-\max}$ are ETL's minimum and maximum optical power.

2.3 | Illumination path design

Figure 3 shows the exact illumination path for the HiLo microscopy. The light guide's light must be collimated, and the final beam diameter D should fill the DMD's active area. Furthermore, this diameter D cannot be too large to prevent illumination energy loss. Therefore, D is the diagonal length of DMD's active area. With the Köhler setup providing high-quality illumination, the collector L1 conveys light from the light guide to the front focal plane of the condenser L2, which collimates light to the DMD. To choose appropriate elements for L1 and L2, we can find the relationship between the illumination half angle u and D. The magnification of the collector (L1) can be calculated as:

$$m_c = \frac{n_1 \sin u}{n_1' \sin u'}, \quad (7)$$

where n_1 and n_1' are the refractive indices in the object and image space of L1, respectively. When the light is collimated by L2, the relationship between u' and D is:

$$\sin u' = \sin\left[\arctan\left(\frac{D}{2f_{condenser}}\right)\right], \quad (8)$$

where $f_{condenser}$ is L2's focal length. The medium is air. Combining Equations (7) and (8) to obtain:

$$\sin u = m_c \sin\left[\arctan\left(\frac{D}{2f_{condenser}}\right)\right], \quad (9)$$

where the angle u can be obtained from experiments (Section 3.2 for detail) and D should be slightly longer than the diagonal length of the DMD active area, which is 12 mm.

2.4 | Smartphone adapter design

We employed CAD design (Autodesk, Inventor Professional 2020) and 3D-printed two adaptors. Figure 4A shows the connections between these adaptors. Two holders were designed to accommodate the iPhone. These adapters are similar to the Thorlabs cage system adapter, so the smartphone can be easily combined with the microscope's main body without losing any concentricity. Figure 4B illustrates the smartphone holder with the light guide and the reversed smartphone lens.

2.5 | HiLo algorithms

The detailed theoretical principle of HiLo has been derived by Mertz et al.[23–25,56,57] Briefly, in HiLo, we use two images captured under uniform and structured illumination to extract the in-focus high-frequency components and in-focus low-frequency components and generate an optically sectioned image $I_{HiLo}(x, y)$:

$$I_{HiLo}(x, y) = \eta I_{Lo}(x, y) + I_{Hi}(x, y), \quad (10)$$

where $I_{HiLo}(x, y)$ is the in-focus low-frequency image and $I_{Hi}(x, y)$ is the in-focus high-frequency image, and x and y are the spatial coordinates at the image plane. The parameter η is used to avoid the discontinuity at all frequencies, calculated by[34]:

$$\eta = \frac{HP_{Kc}}{LP_{Kc}}, \quad (11)$$

where HP_{Kc} and LP_{Kc} are the Gaussian high- and low-pass filters in the spatial frequency domain.[58] They are step functions and have the same cutoff frequency K_c. Here, K_c is equal to the frequency of the structured illumination pattern.[34]

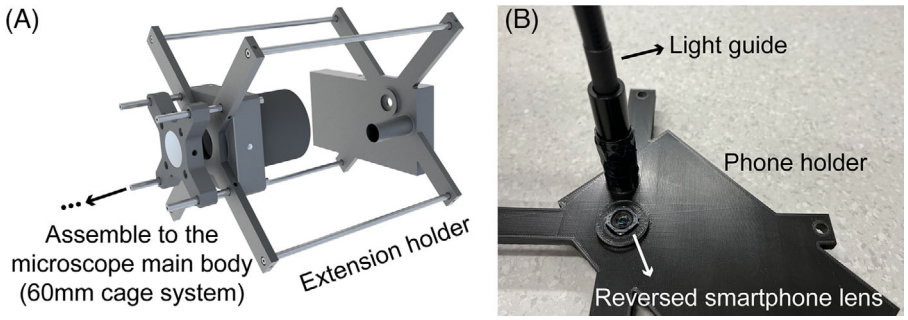

FIGURE 4 Home-made adaptors. (A) The diagram of harnessing the smartphone to the microscope's main body. (B) The light guide and the reversed smartphone lens are aligned through the smartphone holder.

According to the widefield microscope's optical transfer function (OTF), high-frequency features decay rapidly, defocused from the image plane.[59] Thus, we can apply a high-pass filter on the uniformly illuminated image to obtain in-focus high-frequency components:

$$I_{Hi}(x,y) = \mathcal{F}^{-1}\{HP_{Kc}\{\mathcal{F}[I_u(x,y)]\}\}, \tag{12}$$

where $\mathcal{F}$ and $\mathcal{F}^{-1}$ are two-dimensional Fourier and inverse Fourier transform, respectively. HP_{Kc} denotes a Gaussian high-pass filter with the cutoff frequency Kc. I_u is the image under uniform illumination, and it can be divided into the in-focus term I_{focus}, and the defocused term $I_{defocus}$:

$$I_u(x,y) = I_{focus}(x,y) + I_{defocus}(x,y). \tag{13}$$

Similarly, the structurally illuminated image under sinusoidal illumination is:

$$I_s(x,y) = I_{focus}(x,y) + M\sin(2\pi kx) I_{focus}(x,y) + I_{defocus}(x,y), \tag{14}$$

where M is the modulation depth and k is the pattern spatial frequency. The sinusoidal pattern modulates the in-focus images, but not the defocused images.

To extract the in-focus low-frequency components from $I_u(x,y)$, we should use a weighting function to reject defocused low-frequency components. Since the image modulated by the sinusoidal pattern has the maximum contrast at the focal plane, we can relate this weighting function with the contrast. This weighting function can be derived from the rectified subtraction method,[28] the single-sideband demodulation method,[34] and the local contrast method.[24] To remove the sample-induced contrast and obtain a better axial resolution, we can use the difference image with a band-pass filter for the contrast[31]:

$$C(x,y) = std\left\langle \mathcal{F}^{-1}\{BPF\{F[|I_u(x,y) - I_s(x,y)|]\}\}\right\rangle, \tag{15}$$

where std represents the standard deviation operation and BPF is a 2D Gaussian band-pass filter. The band-pass filter removes the DC intensity components. We can enhance the optical sectioning performance of low-frequency components by tuning the band-pass filter's width, and it can be denoted as:

$$BPF(k_x,k_y) = \exp\left(-\frac{k_x^2+k_y^2}{2\sigma^2}\right) - \exp\left(-\frac{k_x^2+k_y^2}{\sigma^2}\right), \tag{16}$$

where (k_x, k_y) is the spectral coordinate and σ is the band-pass filter's width.

We can obtain weighted uniformly illuminated images without $I_{defocus}$ by multiplying the uniformly illuminated image with $C(x,y)$. Then, we apply a low-pass filter to the weighted uniformly illuminated image to diminish the structural-illumination-induced sinusoidal noise and reconstruct the in-focus low-frequency components:

$$I_{Lo}(x,y) = \mathcal{F}^{-1}\{LP_{Kc}\{\mathcal{F}[C(x,y)I_u(x,y)]\}\}, \tag{17}$$

where LP_{Kc} is the low-pass filter with cutoff frequency Kc.

3 | RESULTS

3.1 | Performance of the axial scanning

The theoretical axial scanning range can be obtained from Equation (6). The effective ETL current (I) ranges from -250 mA to 250 mA, corresponding to the optical power from −3.3 to 3.5 dpt. The lateral magnification of the lens pair OL-RL1 is 11.1, and the optical power of RL2 is 10 dpt. The theoretical axial scanning range is 561 μm.

The experimental axial scanning range was measured to compare with the theoretical results. We uploaded a uniform pattern onto the DMD to generate widefield illumination. A resolution target (R3L3S5P, Thorlabs) was imaged at the different axial positions by changing ETL's current (I = −250, −125, 0, 125, and 250 mA) and the

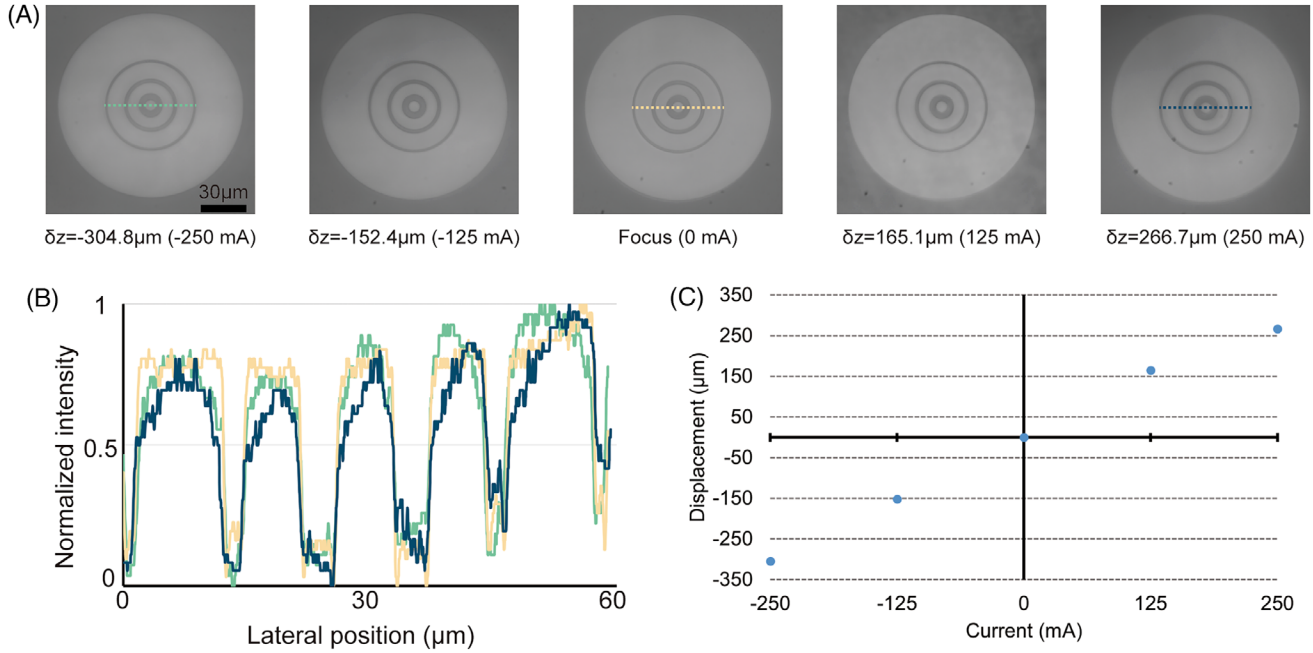

FIGURE 5 Performance of axial scanning and telecentric property. (A) In-focus images at different depths. The ETL current is first changed, and then the target is moved axially to acquire a clear picture. (B) Corresponding line profiles in (A). (C) Relationship between the ETL current and axial displacement.

z-axis translation stage. After each current adjustment, we axially moved the target by changing the translation stage (Vertical Translation Stages, Edmund Optics) to obtain a clear image, and the relationship between I and the axial displacement (d) can be derived (Figure 5C). The translation stage is for finding the relationship between the axial movement and the ETL current.

Figure 5A shows five in-focus images at different depths; the central image is the in-focus image without tuning the I (0 mA). All images were captured without any horizontal or vertical movements. To prove the telecentric property of the proposed system during axial scanning, as shown in Figure 5A, we traced three line profiles at the same position when I were −250, 0, and 250 mA. As shown in Figure 5B, the size of each circle was the same, meaning that the lateral magnification was constant. Figure 5C shows the ETL current versus the axial displacement. We set the axial position when $I = 0$ mA as a reference plane (d is zero). The measured axial scanning range is 571.5 μm, close to the theoretical value of 561 μm with a 2% error.

3.2 | Characterisation of the illumination path

3.2.1 | Radial intensity distribution

According to Equation (9), the light source's radial intensity distribution decides how to choose the optical components to illuminate the whole DMD area with the appropriate beam diameter. We connected the low-loss liquid light guide (5 mm × 6' UV, Edmund Optics) to the smartphone's LED and tested the output illumination radial intensity distribution, as shown in Figure 6C. We also compared the radial intensity distribution directly irradiated from the smartphone shown in Figure 6A. Figure 6B and D shows the corresponding distributions in the polar coordinate system. The light guide can easily guide the illumination source to the aimed position. Besides, the power distribution from the light guide is more focused (14.2° FWHM) than the phone LED (21.6° FWHM).

3.2.2 | Spectral intensity distribution

We used the spectrometer (HR2000, Ocean Optics) to test the smartphone LED's spectrum (Figure 7). Like most white LEDs, the peak emission appears at ~450 nm wavelength, and the normalised intensity in the visible spectrum range is higher than 50% except the dip around 480 nm.

3.3 | Optical sectioning capability

To test SOS' optical sectioning capability, we put a silver-coated mirror (PFR10-P01, Thorlabs) on the sample stage and projected DMD patterns with different periods to its

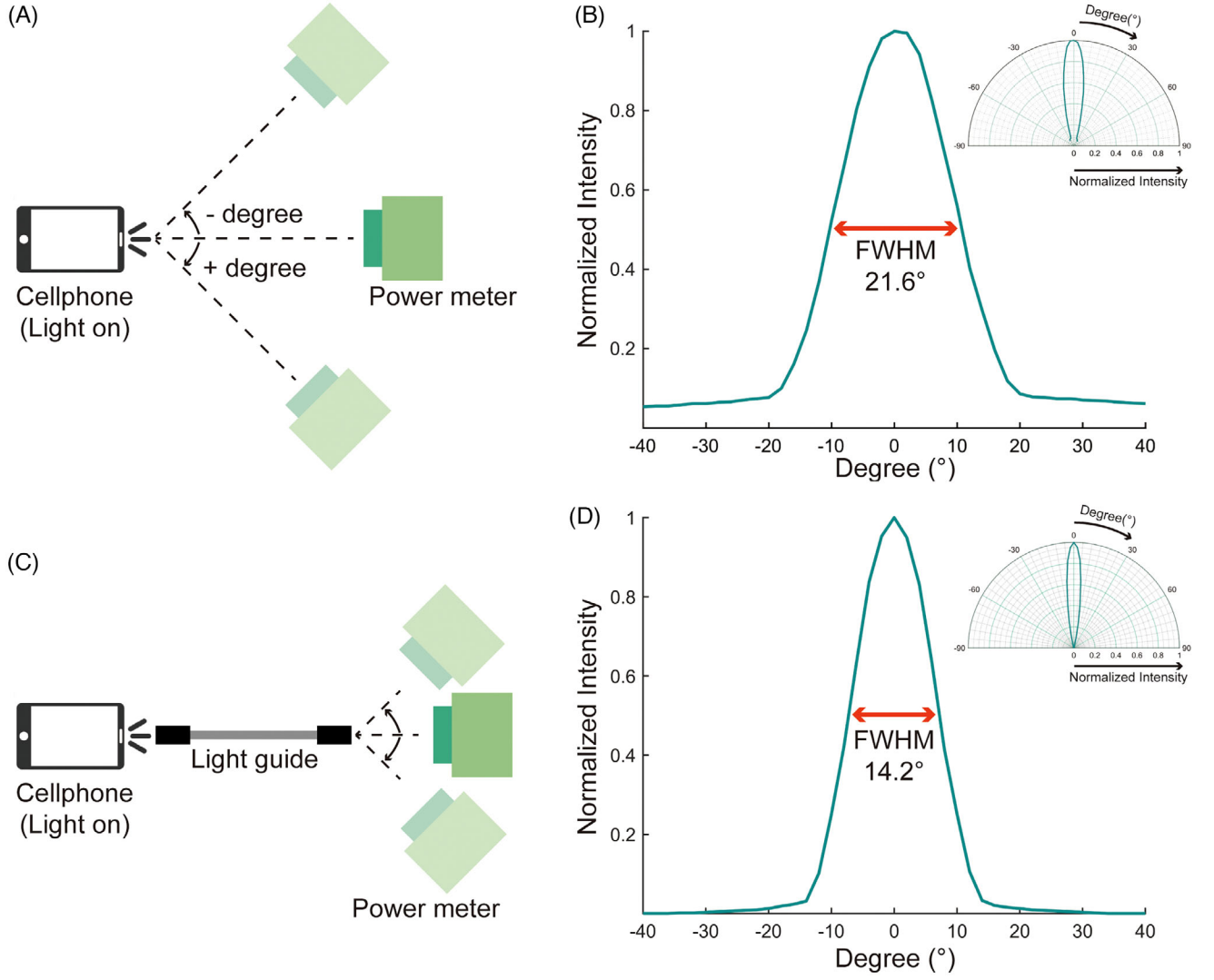

FIGURE 6 The measured radial intensity distribution by the power meter (LASERPOINT, Italy). Intensity distribution tests without (A) and with (C) the light guide. (B) The distribution of (A). (D) The distribution of (C). FWHM means the full width at half-maximum. The subplots in (B) and (D) are in the polar coordinate system.

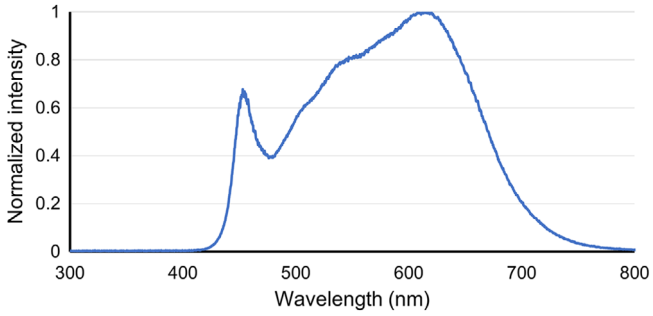

FIGURE 7 The spectrum of the iPhone 13pro LED.

surface. Since the pattern contrast decreased with defocus, we extracted contrast maps from pattern images and quantified the optical sectioning capability accordingly.[28] We used green light (532 nm) as a reference.[60] An emission filter (FL532-3, Thorlabs) was inserted before the liquid guide. The focal plane was axially scanned with a 5 μm step for a 15.12 μm/lp pattern and a 10 μm step for 75.6 and 241.92 μm/lp patterns. The normalised contrast for each axial image is calculated by[26]:

$$C = \frac{I_{\max} - I_{\min}}{I_{\max} + I_{\min}}, \tag{18}$$

where the $I_{\max}$ and the $I_{\min}$ are the maximum and the minimum intensity of the images of the projected patterns.

Figure 8A shows the relationship between the normalised contrast and the axial position for three patterns with different frequencies. A higher frequency shows better optical sectioning capability. This is because the higher spatial frequency modulation of the OTF in widefield microscopy decays with defocus more quickly, enabling

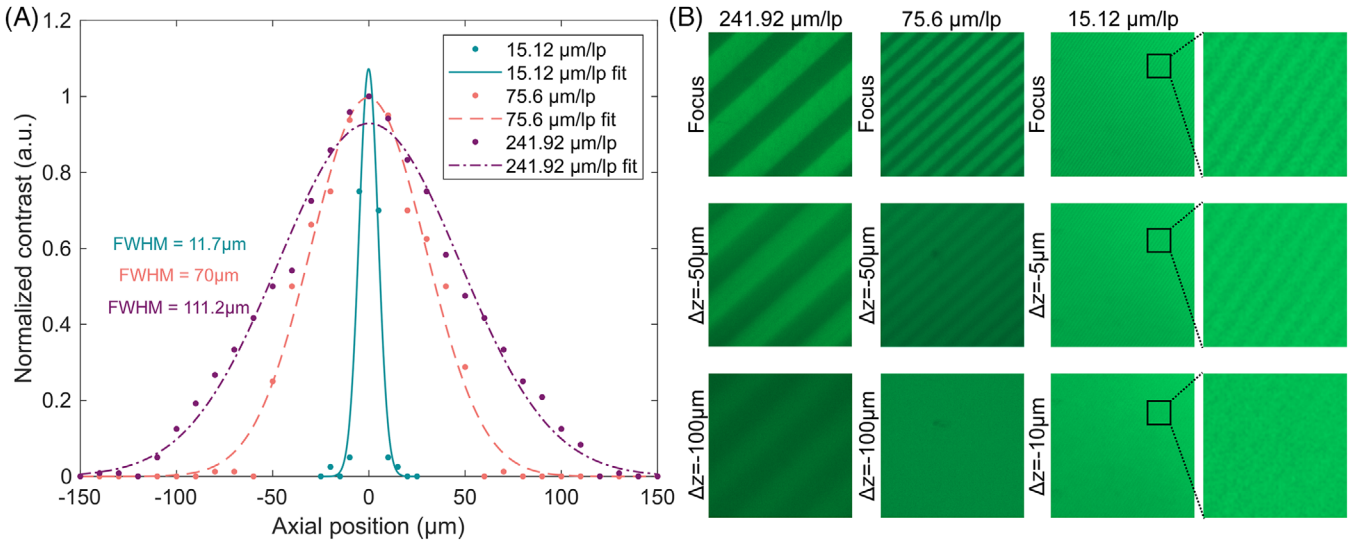

FIGURE 8 SOS' optical sectioning capability. (A) The axial contrast profiles of DMD patterns for three spatial frequencies were obtained by imaging the reflected signal from the mirror sample. We used the Gaussian function for each experimental dataset. The Gaussian function's FWHM is also shown. (B) The images with three frequencies in (A) are captured at focus and two defocus planes.

better optical sectioning power. In this study, the DMD's pixel size is 7.56 μm, so the highest frequency is 15.12 μm/lp. Figure 8B shows images with three frequencies captured at three axial positions. The pattern structure at 15.12 μm/lp almost vanishes when the defocus distance is −10 μm, whereas the periodic structure at 241.92 μm/lp is still observable at the defocus distance −100 μm.

3.4 | Fluorescent beads imaging

We used three fluorescent beads with 465, 515, and 605 nm emission wavelengths (FluoSpheres, Thermo Fisher) to test SOS' imaging performances. The bead's diameter was 10 μm. The samples were diluted 10 times with deionised water and set on microscopic glass slides. For structured illumination, the DMD pattern period was set to 6 pix/lp (45.36 μm/lp). For uniform illumination, all pixels on DMD were turned 'on'. Figure 9 shows the captured images of the fluorescent bead samples. The widefield images were imaged under uniform illumination, and the SI images were under structured illumination. We used the HiLo algorithm to obtain the final HiLo images. To excite different fluorescent beads, we inserted different optical filters into the illumination path, as shown in Figure 1A, letter F (Figure 9A, FBH430-10; Figure 9B, FBH500-40; Figure 9C, FBH580-10, Thorlabs). Because of the Bayer filter on the smartphone sensor, emission filters are unnecessary. Figure 9D–F shows corresponding line profiles in Figure 9A–C.

To test SOS' optical sectioning performances, the fluorescent beads (FluoSpheres, Thermo Fisher, 505/515) of different layers were optically sectioned and imaged. We dipped the 10 μL bead solution without dilution onto the microscopic glass side and waited until it was dry. The current of the ETL was set to −10.5, −7.0, −3.5, 0.0, 3.5, 7.0 mA, and the focus plane from −15 to -10 μm with a 5 μm step. At each step, beads were illuminated by uniform and structured illumination (45.36 μm/lp). Figure 10 shows widefield, structured illumination, and HiLo-processed images of accumulated beads at different depths. The HiLo images show much better optical sectioning capacity compared with widefield images. Out-of-focus signals are significantly suppressed. Several artefacts in the final HiLo images can also be found in the same position as widefield images (red rectangular), and there is no such artefact when samples are sparse (Figure 9). More discussion about this effect can be found in Section 4.

4 | DISCUSSIONS AND FUTURE ASPECTS

In resource-limited areas, using microscopes for biomedical research and disease diagnosis is costly, especially for advanced optical sectioning microscopes equipped with high-performance light sources, scientific sensors, precise translation stages and other optical components. This article presents the first smartphone-based HiLo optical sectioning microscope, which replaces the CMOS sensor and the light source in a traditional HiLo microscope with a single smartphone. Table 1 summarises the components used in our SOS or traditional HiLo and the corresponding costs. If the other components (objective lens, mirror, cage

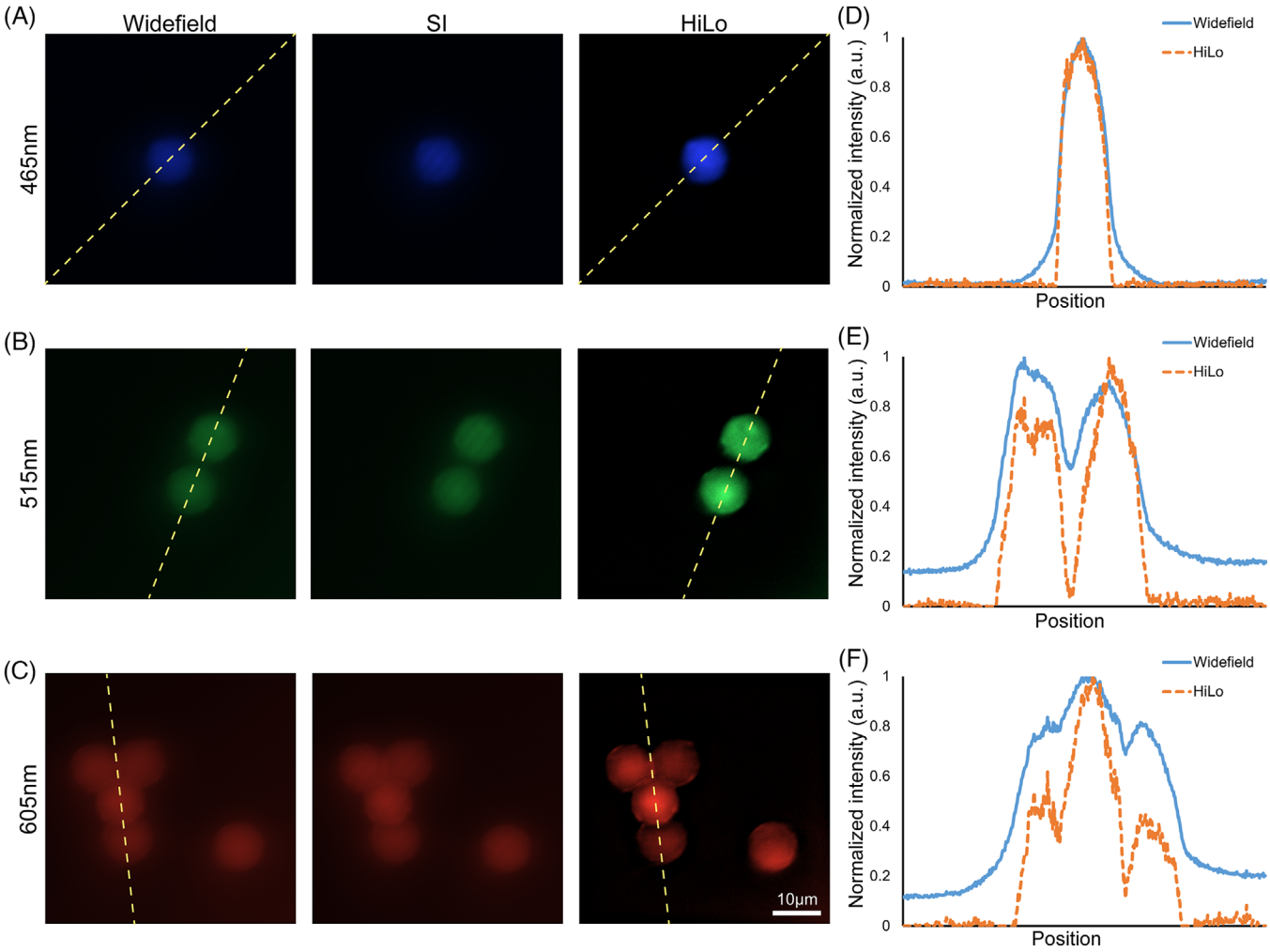

FIGURE 9 Fluorescent bead images at different wavelengths. (A) The bead samples with 430 nm excitation and 465 nm emission. (B) The bead samples with 505 nm excitation and 515 nm emission. (C) The bead samples with 580 nm excitation and 605 nm emission. Corresponding line profiles of widefield and HiLo images are shown in (D)–(F). SI: Structured illumination.

rod, lenses, filter) in SOS and traditional HiLo systems are identical, SOS costs ~ £1965 and the traditional HiLo costs ~ £9000. This study paves the way for developing low-cost portable HiLo microscopy systems.

SOS's main structure was designed and built using the compact cage system. We designed and fabricated adapters to combine the smartphone with the cage structure. We used a liquid light guide to guide the smartphone torch's light to the DMD for structured illumination. The advantage of this approach is that we can freely guide light by using the liquid light guide to the aimed position with a negligible loss. In this study, we only test the radial intensity distribution because the aim is to quickly demonstrate our proof-of-concept prototype and determine appropriate lenses for collimation so that the collimated beam size can exactly cover the DMD's effective area. However, to examine whether the illumination source can effectively excite biological fluorescent dyes, the light power output and the Etendue of the light coming out of the fibre still need to be carefully examined. These aspects are out of the scope of this work, and we will provide quantitative studies soon.

The ETL in our SOS is an axial scanner for selecting sample planes and adjusting the focal plane. The ETL is conjugated to the BPP of the objective lens by a 4f configuration. This telecentric setup can maintain the lateral magnification regardless of the axial plane's position. Therefore, the field of view and the resolution are maintained. Moreover, Z-stack images can be directly generated without any postprocessing. The broadband LED light source can effectively excite different PS beads.

The proof-of-concept SOS prototype can successfully realise the optical sectioning function and image 10 μm PS fluorescent beads, meaning that it has the potential to image more sophisticated fluorescently labelled biological samples. However, as discussed in Section 3.5, artefacts can be found in the final HiLo results when fluorescent

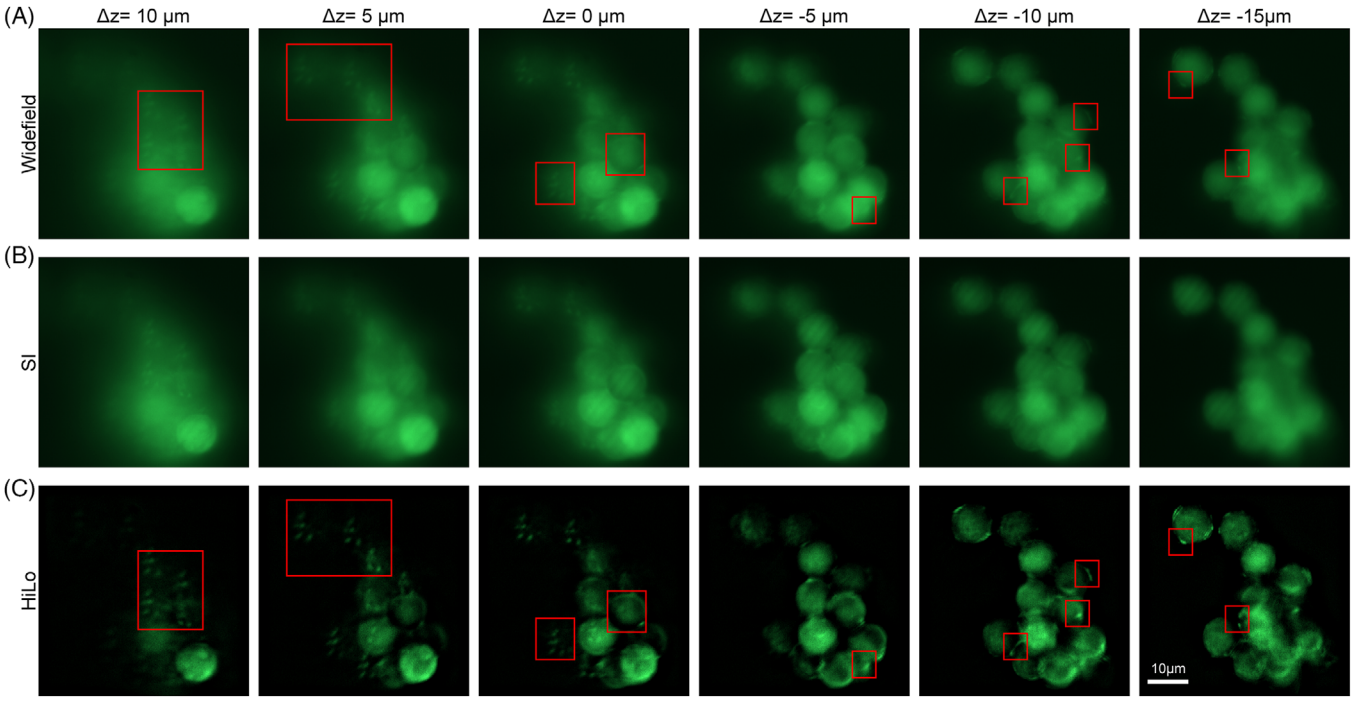

FIGURE 10 Images of accumulated fluorescent beads at different depths. (A) widefield images. (B) SI images. (C) HiLo-processed images.

TABLE 1 Costs of the proposed SOS and traditional HiLo systems.

	SOS	Traditional HiLo
Light source	N/A	Tungsten-Halogen Source: ~ £5000
Camera sensor	N/A	12 MP colour CMOS camera: ~ £2000
Smartphone	Iphone 13pro: ~ £615	N/A
Light guide	~ £400	N/A
Axial translation stage	Electrically tuneable lens: ~ £950	Motorised translation stage: ~ £2000
	Total: ~ £1965	Total: ~ £9000

beads are too dense. We conclude that the illumination and sample properties cause these artefacts. In addition, the images captured by the iPhone are usually already post-processed by embedded algorithms. Therefore, artefacts may be introduced when the processed images are further processed by the HiLo algorithms. Shi et al.[26] also discovered these artefacts in their experiments. They concluded that these artefacts can be avoided by carefully choosing appropriate patterns and the frequency of the structure illumination according to biological samples. However, the cause of these artefacts is still unknown and needs further examination. In future studies, we will examine this aspect thoroughly. We will also use Android smartphones and develop software to acquire raw format photos to discuss artefact problems.

This report presents a fast proof-of-concept study, and we will conduct biological experiments soon to examine how well SOS can image actual biological samples (such as fluorescently labelled zebrafish). To develop a compact portable SOS, we will 3D print or manufacture component holders instead of using Thorlabs cage systems.

This is a pioneer study about using smartphones instead of light sources and cameras to realise HiLo optical sectioning microscopy. The cost is lower than that of traditional HiLo microscopy. However, we aim to minimise further its cost in the future. The most expensive parts of SOS are the DMD and the light guide. To save money and enable HiLo in low-resource settings, we can substitute the DMD with the diffusive or periodic pattern glass plates, and the light guide can be easily fabricated by low-cost polymers such as PDMS or PMMA. Furthermore, micro-LEDs are broadly used for illumination and display because of their brightness and small volume. We can use a micro-LED mini display and cheaper relay optics to generate and relay structured illumination. If this method is cheaper, additional light sources and light guides can be replaced, and more illumination structures can be generated by using a computer to control the micro-LED mini display.

The ETL and telecentric design maintain the lateral magnification and fast axial scanning. However, an ETL still costs nearly £950, which is expensive for laboratories without sufficient funds. Cicuta et al.[61] developed an open-source microscope, OpenFlexure, which allows easy customisation and fast development of low-cost microscopes. For instance, Stirling et al.[62] used the OpenFlexure Delta Stage and developed a multimodal microscope. Matsui et al.[63] established an optical sectioning microscope with the OpenFlexure stage. The other open-source microscope project, UC2,[64,65] also provides good options for customising low-cost microscopes. Therefore, in our future studies, we will fully use these platforms and create appropriate modules to replace the ETL.

Considering the fast development of smartphones, the iPhone 13Pro will eventually need to be updated, and using advanced smartphones in resource-limited areas is also unrealistic. To leverage the limitations of our smartphone HiLo and expand its application scenarios, we will focus on making it more general in future. For 3D-printed adapter parts, we will design a more compact and general part for different smartphones. We will apply clutch structures and adjustable mechanisms into adapters to harness different smartphones seamlessly. In this study, there is only one adapter that simultaneously combines the light guide and an iPhone 13 Pro. Considering that the cellphone's LED torch varies from type to type, we will separate the adapter into two parts, one for the smartphone's main body and the other for the light guide. Users can harness the phone and light guide to their corresponding adapters and combine two adapters. This configuration can make our method more general without considering smartphone types.

In conclusion, this is a proof-of-concept study that tests the possibility of using smartphones to realise HiLo optical sectioning microscopy. SOS's performance and configuration can still be further enhanced in the future. Once the limitations are solved, and portable, low-cost HiLo microscopes will be developed soon.

5 | CONCLUSION

We demonstrated a smartphone-based optical sectioning (SOS) microscope based on the HiLo principle. Compared with traditional HiLo, it can save more than £7000 in components. In SOS, the illumination source and camera sensor can be realised by a smartphone. We used an ETL for the axial translation stage, realising axial scanning and focus plane selection. The telecentric setup can maintain the lateral magnification regardless of the axial plane's position, and postprocessing for imaging registration is not required. SOS offers a 571.5 μm axial range, close to the theoretical value (561 μm) with a 2% error. The axial resolution can reach 11.7 μm. We successfully used SOS to image different PS beads attached to the coverslip, and the optically sectioned images of beads in 3D suspension were also recorded in the 25 μm axial range with a 5 μm step.

AUTHOR CONTRIBUTIONS

Ziao Jiao: Investigation; conceptualisation; validation; hardware design; sample preparation; data analysis; article writing and editing. **Mingliang Pan**: Hardware design; data analysis. **Khadija Yousaf** and **Daniel Doveiko**: Sample preparation. **Michelle Maclean** and **David Griffin**: Spectrum testing. **Yu Chen**: Sample preparation and supervision. **David Day Uei Li**: Project supervision & administration; concept presentation; article writing and editing & funding acquisition.

ACKNOWLEDGEMENTS

The research has been supported by the Engineering and Physical Sciences Research Council under EPSRC Grant: EP/L01596X/1, the Royal Society of Edinburgh, and the China Scholarship Council. Daniel Doveiko would like to thank PQ Corporation and EPSRC for the PhD studentship (2629179).

CONFLICT OF INTEREST STATEMENT

The authors declare no conflicts of interest.

ORCID

Ziao Jiao https://orcid.org/0009-0005-8067-1238
Daniel Doveiko https://orcid.org/0000-0002-0516-689X

REFERENCES

1. Webb, D. J., & Brown, C. M. (2013). Epi-fluorescence microscopy. *Methods in Molecular Biology (Clifton, N.J.)*, *931*, 29–59.
2. Schneckenburger, H., Weber, P., Wagner, M., Schickinger, S., Richter, V., Bruns, T., Strauss, W. S. L., & Wittig, R. (2012). Light exposure and cell viability in fluorescence microscopy. *Journal of Microscopy*, *245*(3), 311–318.
3. Icha, J., Weber, M., Waters, J. C., & Norden, C. (2017). Phototoxicity in live fluorescence microscopy, and how to avoid it. *BioEssays*, *39*(8), 1700003.
4. Gustafsson, M. G. L., Shao, L., Carlton, P. M., Wang, C. J. R., Golubovskaya, I. N., Cande, W. Z., Agard, D. A., & Sedat, J. W. (2008). Three-dimensional resolution doubling in wide-field fluorescence microscopy by structured illumination. *Biophysical Journal*, *94*(12), 4957–4970.
5. Agard, D. A., Hiraoka, Y., Shaw, P., & Sedat, J. W. (1989). Fluorescence microscopy in three dimensions. *Methods in Cell Biology*, *30*, 353–377.
6. Amos, W. B., & White, J. G. (2003). How the confocal laser scanning microscope entered biological research. *Biology of the Cell*, *95*(6), 335–342.
7. Carlsson, K., Danielsson, P. E., Liljeborg, A., Majlöf, L., Lenz, R., & Åslund, N. (1985). Three-dimensional microscopy using a confocal laser scanning microscope. *Optics Letters*, *10*(2), 53–55.

8. Bayguinov, P. O., Oakley, D. M., Shih, C.-C., Geanon, D. J., Joens, M. S., & Fitzpatrick, J. A. J. (2018). Modern laser scanning confocal microscopy. *Current Protocols in Cytometry*, *85*(1), e39.
9. Dusch, E., Dorval, T., Vincent, N., Wachsmuth, M., & Genovesio, A. (2007). Three-dimensional point spread function model for line-scanning confocal microscope with high-aperture objective. *Journal of Microscopy*, *228*(2), 132–138.
10. Gareau, D. S., Krueger, J. G., Hawkes, J. E., Lish, S. R., Dietz, M. P., Mülberger, A. G., Mu, E. W., Stevenson, M. L., Lewin, J. M., Meehan, S. A., & Carucci, J. A. (2017). Line scanning, stage scanning confocal microscope (LSSSCM). *Biomedical Optics Express*, *8*(8), 3807–3815.
11. So, P T. C., Dong, C Y., Masters, B R., & Berland, K M. (2000). Two-photon excitation fluorescence microscopy. *Annual Review of Biomedical Engineering*, *2*(1), 399–429.
12. Helmchen, F., & Denk, W. (2005). Deep tissue two-photon microscopy. *Nature Methods*, *2*(12), 932–940.
13. Moreaux, L., Sandre, O., Blanchard-Desce, M., & Mertz, J. (2000). Membrane imaging by simultaneous second-harmonic generation and two-photon microscopy. *Optics Letters*, *25*(5), 320–322.
14. Olarte, O. E., Andilla, J., Gualda, E. J., & Loza-Alvarez, P. (2018). Light-sheet microscopy: A tutorial. *Advances in Optics and Photonics*, *10*(1), 111–179.
15. Pitrone, P. G., Schindelin, J., Stuyvenberg, L., Preibisch, S., Weber, M., Eliceiri, K. W., Huisken, J., & Tomancak, P. (2013). OpenSPIM: An open-access light-sheet microscopy platform. *Nature Methods*, *10*(7), 598–599.
16. Vettenburg, T., Dalgarno, H. I. C., Nylk, J., Coll-Lladó, C., Ferrier, D. E. K., Čižmár, T., Gunn-Moore, F. J., & Dholakia, K. (2014). Light-sheet microscopy using an Airy beam. *Nature Methods*, *11*(5), 541–544.
17. Jemielita, M., Taormina, M. J., Delaurier, A., Kimmel, C. B., & Parthasarathy, R. (2013). Comparing phototoxicity during the development of a zebrafish craniofacial bone using confocal and light sheet fluorescence microscopy techniques. *Journal of Biophotonics*, *6*(11-12), 920–928.
18. Xiong, B., Han, X., Wu, J., Xie, H., & Dai, Q. (2020). Improving axial resolution of Bessel beam light-sheet fluorescence microscopy by photobleaching imprinting. *Optics Express*, *28*(7), 9464–9476.
19. Chen, B.-C., Legant, W. R., Wang, K., Shao, L., Milkie, D. E., Davidson, M. W., Janetopoulos, C., Wu, X. S., Hammer, J. A., Liu, Z., English, B. P., Mimori-Kiyosue, Y., Romero, D. P., Ritter, A. T., Lippincott-Schwartz, J., Fritz-Laylin, L., Mullins, R. D., Mitchell, D. M., Bembenek, J. N., … Betzig, E. (2014). Lattice light-sheet microscopy: imaging molecules to embryos at high spatiotemporal resolution. *Science*, *346*(6208), 1257998.
20. Gustafsson, M. G. L. (2000). Surpassing the lateral resolution limit by a factor of two using structured illumination microscopy. *Journal of Microscopy*, *198*(2), 82–87.
21. York, A. G., Parekh, S. H., Nogare, D. D., Fischer, R. S., Temprine, K., Mione, M., Chitnis, A. B., Combs, C. A., & Shroff, H. (2012). Resolution doubling in live, multicellular organisms via multifocal structured illumination microscopy. *Nature Methods*, *9*(7), 749–754.
22. Dan, D., Lei, M., Yao, B., Wang, W., Winterhalder, M., Zumbusch, A., Qi, Y., Xia, L., Yan, S., Yang, Y., Gao, P., Ye, T., & Zhao, W. (2013). DMD-based LED-illumination super-resolution and optical sectioning microscopy. *Scientific Reports*, *3*(1), 1116.
23. Ventalon, C., & Mertz, J. (2006). Dynamic speckle illumination microscopy with translated versus randomized speckle patterns. *Optics Express*, *14*(16), 7198–7209.
24. Lim, D., Chu, K. K., & Mertz, J. (2008). Wide-field fluorescence sectioning with hybrid speckle and uniform-illumination microscopy. *Optics Letters*, *33*(16), 1819–1821.
25. Lim, D., Ford, T. N., Chu, K. K., & Metz, J. (2011). Optically sectioned in vivo imaging with speckle illumination HiLo microscopy. *Journal of Biomedical Optics*, *16*(1), 016014–016014.
26. Shi, R., & Kong, L. (2021). Evaluating structured-illumination patterns in optimizing optical-sectioning of HiLo microscopy. *Journal of Physics D: Applied Physics*, *54*(41), 414001.
27. Chai, C., Chen, C., Liu, X., & Lei, Z. (2021). Deep learning based one-shot optically-sectioned structured illumination microscopy for surface measurement. *Optics Express*, *29*(3), 4010–4021.
28. Ford, T. N., Lim, D., & Mertz, J. (2012). Fast optically sectioned fluorescence HiLo endomicroscopy. *Journal of Biomedical Optics*, *17*(2), 021105–021105.
29. Choi, H., Wadduwage, D. N., Tu, T. Y., Matsudaira, P., & So, P. T. C. (2015). Three-dimensional image cytometer based on wide-field structured light microscopy and high-speed remote depth scanning. *Cytometry Part A*, *87*(1), 49–60.
30. Lauterbach, M. A., Ronzitti, E., Sternberg, J. R., Wyart, C., & Emiliani, V. (2015). Fast calcium imaging with optical sectioning via HiLo microscopy. *PloS One*, *10*(12), e0143681.
31. Shi, R., Jin, C., Xie, H., Zhang, Y., Li, X., Dai, Q., & Kong, L. (2019). Multi-plane, wide-field fluorescent microscopy for biodynamic imaging in vivo. *Biomedical Optics Express*, *10*(12), 6625–6635.
32. Michaelson, J., Choi, H., So, P., & Huang, H. (2012). Depth-resolved cellular microrheology using HiLo microscopy. *Biomedical Optics Express*, *3*(6), 1241–1255.
33. Zhou, X., Bedggood, P., & Metha, A. (2014). Improving high resolution retinal image quality using speckle illumination HiLo imaging. *Biomedical Optics Express*, *5*(8), 2563–2579.
34. Santos, S., Chu, K. K., Lim, D., Bozinovic, N., Ford, T. N., Hourtoule, C., Bartoo, A. C., Singh, S. K., & Mertz, J. (2009). Optically sectioned fluorescence endomicroscopy with hybrid-illumination imaging through a flexible fiber bundle. *Journal of Biomedical optics*, *14*(3), 030502–030502.
35. Mertz, J., & Kim, J. (2010). Scanning light-sheet microscopy in the whole mouse brain with HiLo background rejection. *Journal of Biomedical Optics*, *15*(1), 016027–016027.
36. Bhattacharya, D., Singh, V. R., Zhi, C., So, P. T. C., Matsudaira, P., & Barbastathis, G. (2012). Three dimensional HiLo-based structured illumination for a digital scanned laser sheet microscopy (DSLM) in thick tissue imaging. *Optics Express*, *20*(25), 27337–27347.
37. Sung, Y., Campa, F., & Shih, W.-C. (2017). Open-source do-it-yourself multi-color fluorescence smartphone microscopy. *Biomedical optics express*, *8*(11), 5075–5086.
38. Dai, B., Jiao, Z., Zheng, L., Bachman, H., Fu, Y., Wan, X., Zhang, Y., Huang, Y., Han, X., Zhao, C., Huang, T. J., Zhuang, S., & Zhang, D. (2019). Colour compound lenses for a portable fluorescence microscope. *Light: Science & Applications*, *8*(1), 75.

39. De Haan, K., Ceylan Koydemir, H., Rivenson, Y., Tseng, D., Van Dyne, E., Bakic, L., Karinca, D., Liang, K., Ilango, M., Gumustekin, E., & Ozcan, A. (2020). Automated screening of sickle cells using a smartphone-based microscope and deep learning. *NPJ digital medicine*, *3*(1), 76.
40. Gopinath, S. C. B., Tang, T.-H., Chen, Y., Citartan, M., & Lakshmipriya, T. (2014). Bacterial detection: From microscope to smartphone. *Biosensors and Bioelectronics*, *60*, 332–342.
41. Chung, S., Breshears, L. E., Gonzales, A., Jennings, C. M., Morrison, C. M., Betancourt, W. Q., Reynolds, K. A., & Yoon, J.-Y. (2021). Norovirus detection in water samples at the level of single virus copies per microliter using a smartphone-based fluorescence microscope. *Nature Protocols*, *16*(3), 1452–1475.
42. Ayardulabi, R., Khamespanah, E., Abbasinia, S., & Ehtesabi, H. (2021). Point-of-care applications of smartphone-based microscopy. *Sensors and Actuators A: Physical*, *331*, 113048.
43. Cai, F., Wang, T., Lu, W., & Zhang, X. (2020). High-resolution mobile bio-microscope with smartphone telephoto camera lens. *Optik*, *207*, 164449.
44. Müller, V., Sousa, J. M., Ceylan Koydemir, H., Veli, M., Tseng, D., Cerqueira, L., Ozcan, A., Azevedo, N. F., & Westerlund, F. (2018). Identification of pathogenic bacteria in complex samples using a smartphone based fluorescence microscope. *RSC Advances*, *8*(64), 36493–36502.
45. Vietz, C., Schütte, M. L., Wei, Q., Richter, L., Lalkens, B., Ozcan, A., Tinnefeld, P., & Acuna, G. P. (2019). Benchmarking smartphone fluorescence-based microscopy with DNA origami nanobeads: Reducing the gap toward single-molecule sensitivity. *ACS Omega*, *4*(1), 637–642.
46. Meng, X., Huang, H., Yan, K., Tian, X., Yu, W., Cui, H., Kong, Y., Xue, L., Liu, C., & Wang, S. (2017). Smartphone based hand-held quantitative phase microscope using the transport of intensity equation method. *Lab on a Chip*, *17*(1), 104–109.
47. Jung, D., Choi, J.-H., Kim, S., Ryu, S., Lee, W., Lee, J.-S., & Joo, C. (2017). Smartphone-based multi-contrast microscope using color-multiplexed illumination. *Scientific Reports*, *7*(1), 7564.
48. Rabha, D., Rather, M. A., Mandal, M., & Nath, P. (2022). Programmable illumination smartphone microscopy (PISM): A multimodal imaging platform for biomedical applications. *Optics and Lasers in Engineering*, *151*, 106931.
49. Phillips, Z. F., D'ambrosio, M. V., Tian, L., Rulison, J. J., Patel, H. S., Sadras, N., Gande, A. V., Switz, N. A., Fletcher, D. A., & Waller, L. (2015). Multi-contrast imaging and digital refocusing on a mobile microscope with a domed LED array. *PloS One*, *10*(5), e0124938.
50. Lee, K. C., Lee, K., Jung, J., Lee, S. H, Kim, D., & Lee, S. A. (2021). A smartphone-based Fourier ptychographic microscope using the display screen for illumination. *ACS Photonics*, *8*(5), 1307–1315.
51. Kim, J., Go, T., & Lee, S. J. (2021). Volumetric monitoring of airborne particulate matter concentration using smartphone-based digital holographic microscopy and deep learning. *Journal of Hazardous Materials*, *418*, 126351.
52. Wei, Q., Acuna, G., Kim, S., Vietz, C., Tseng, D., Chae, J., Shir, D., Luo, W., Tinnefeld, P., & Ozcan, A. (2017). Plasmonics enhanced smartphone fluorescence microscopy. *Scientific Reports*, *7*(1), 2124.
53. Koydemir, H. C., Gorocs, Z., Tseng, D., Cortazar, B., Feng, S., Chan, R. Y. L., Burbano, J., Mcleod, E., & Ozcan, A. (2015). Rapid imaging, detection and quantification of *Giardia lamblia* cysts using mobile-phone based fluorescent microscopy and machine learning. *Lab on a Chip*, *15*(5), 1284–1293.
54. Rabha, D., Biswas, S., Chamuah, N., Mandal, M., & Nath, P. (2021). Wide-field multi-modal microscopic imaging using smartphone. *Optics and Lasers in Engineering*, *137*, 106343.
55. Greivenkamp, J. E. (2004). *Field guide to geometrical optics*. SPIE.
56. Ventalon, C., & Mertz, J. (2005). Quasi-confocal fluorescence sectioning with dynamic speckle illumination. *Optics Letters*, *30*(24), 3350–3352.
57. Ventalon, C., Heintzmann, R., & Mertz, J. (2007). Dynamic speckle illumination microscopy with wavelet prefiltering. *Optics Letters*, *32*(11), 1417–1419.
58. Kang, S., Ryu, I., Kim, D., & Kauh, S. K. (2018). High-speed three-dimensional surface profile measurement with the HiLo optical imaging technique. *Current Optics and Photonics*, *2*(6), 568–575.
59. Stokseth, P. A. (1969). Properties of a defocused optical system. *JOSA*, *59*(10), 1314–1321.
60. Kim, J. Y., Lee, C., Park, K., Lim, G., & Kim, C. (2015). Fast optical-resolution photoacoustic microscopy using a 2-axis water-proofing MEMS scanner. *Scientific Reports*, *5*(1), 7932.
61. Collins, J T., Knapper, J., Stirling, J., Mduda, J., Mkindi, C., Mayagaya, V., Mwakajinga, G A., Nyakyi, P T., Sanga, V L., Carbery, D., White, L., Dale, S., Jieh Lim, Z., Baumberg, J J., Cicuta, P., Mcdermott, S., Vodenicharski, B., & Bowman, R. (2020). Robotic microscopy for everyone: The OpenFlexure microscope. *Biomedical Optics Express*, *11*(5), 2447–2460.
62. Mcdermott, S., Ayazi, F., Collins, J., Knapper, J., Stirling, J., Bowman, R., & Cicuta, P. (2022). Multi-modal microscopy imaging with the OpenFlexure Delta Stage. *Optics Express*, *30*(15), 26377–26395.
63. Matsui, T., & Fujiwara, D. (2022). Optical sectioning robotic microscopy for everyone: the structured illumination microscope with the OpenFlexure stages. *Optics Express*, *30*(13), 23208–23216.
64. Wang, H., Lachmann, R., Marsikova, B., Heintzmann, R., & Diederich, B. (2021). UCsim2: 2D structured illumination microscopy using UC2. *bioRxiv*, 2021–2001.
65. Diederich, B., Lachmann, R., Carlstedt, S., Marsikova, B., Wang, H., Uwurukundo, X., Mosig, A. S., & Heintzmann, R. (2020). A versatile and customizable low-cost 3D-printed open standard for microscopic imaging. *Nature Communications*, *11*(1), 5979.

How to cite this article: Jiao, Z., Pan, M., Yousaf, K., Doveiko, D., Maclean, M., Griffin, D., Chen, Y., & Li, D. D. U. (2024). Smartphone-based optical sectioning (SOS) microscopy with a telecentric design for fluorescence imaging. *Journal of Microscopy*, 1–14. https://doi.org/10.1111/jmi.13334